Biophysical Journal Volume 101 September 2011 1522–1528

Superresolution Imaging of Multiple Fluorescent Proteins with Highly Overlapping Emission Spectra in Living Cells

Mudalige S. Gunewardene,[†] Fedor V. Subach,[‡] Travis J. Gould,[†] Gregory P. Penoncello,[†] Manasa V. Gudheti,[†] Vladislav V. Verkhusha,[‡] and Samuel T. Hess[†*]

[†]Department of Physics and Astronomy and Institute for Molecular Biophysics, University of Maine, Orono, Maine; and [‡]Department of Anatomy and Structural Biology and Gruss-Lipper Biophotonics Center, Albert Einstein College of Medicine, Bronx, New York

ABSTRACT Localization-based superresolution optical imaging is rapidly gaining popularity, yet limited availability of genetically encoded photoactivatable fluorescent probes with distinct emission spectra impedes simultaneous visualization of multiple molecular species in living cells. We introduce PAmKate, a monomeric photoactivatable far-red fluorescent protein, which facilitates simultaneous imaging of three photoactivatable proteins in mammalian cells using fluorescence photoactivation localization microscopy (FPALM). Successful probe identification was achieved by measuring the fluorescence emission intensity in two distinct spectral channels spanning only ~100 nm of the visible spectrum. Raft-, non-raft-, and cytoskeleton-associated proteins were simultaneously imaged in both live and fixed fibroblasts coexpressing Dendra2-hemagglutinin, PAmKate-transferrin receptor, and PAmCherry1-β-actin fusion constructs, revealing correlations between the membrane proteins and membrane-associated actin structures.

INTRODUCTION

Until recently, the resolution in conventional far-field fluorescence microscopes has been limited by diffraction to roughly half the detection wavelength. A family of superresolution microscopy methods has successfully surpassed this limitation and is able to laterally resolve objects with resolution of a few tens of nanometers, an improvement of ~10-fold over diffraction-limited resolution (1). Methods utilizing a focused beam at the sample have used interferometric methods or manipulation of probe photophysics to constrain the effective sample illumination or detection volume, thereby enabling objects to be resolved below the diffraction limit (2). Localization-based methods operate typically under widefield or total internal reflection (TIR) illumination and rely on imaging sparse distributions of single molecules (3). Shape analysis of individual single-molecule intensity profiles enables determination of their centers with nanometer precision (4).

Fluorescence photoactivation localization microscopy (FPALM) (5), photoactivated localization microscopy (PALM) (6), and stochastic optical reconstruction microscopy (STORM) (7) were the first localization-based methods to achieve superresolution. Localization methods require the use of fluorescent molecules initially residing in a metastable inactivated state (typically nonfluorescent when detected within a particular range of wavelengths). Molecules are stochastically driven to a highly fluorescent state (typically fluorescent within that same range of wavelengths) at a rate that is controlled optically, and coupled with inherent fluorescent photobleaching to attain sparse distributions of fluorescent molecules present at the sample at any given moment. Although there are different approaches to realize such fluorescent states, FPALM/PALM relies on photoactivatable fluorescent proteins (PAFPs), whereas STORM utilizes conjugated organic dyes that act as molecular switches in the presence of thiol. Most PAFPs are commonly and efficiently activated using violet (~400 nm) light, whereas a more red-shifted illumination wavelength (readout) is typically used to effectively excite fluorescence from the activated molecules. Activation and readout continue until sufficiently large numbers of molecules, or all possible molecules, are imaged. Acquired images are then analyzed to determine individual molecular positions (localizations) and intensities and subsequently used to render a superresolution image. Specific labeling of proteins in biological specimens with PAFPs can be achieved through genetically encoded fusion constructs. Applicable to living cells (8–10) and three-dimensional specimens (11,12), localization microscopy has even evolved to measure single-molecule anisotropies (13) and image multiple species (14–21).

More recent localization-based approaches such as ground-state depletion microscopy followed by individual molecule return (GSDIM) (22), or direct STORM (dSTORM) (23), have achieved superresolution using standard fluorophores by transiently transferring them into a nonfluorescent dark (triplet) state by continuous excitation and imaging sparsely distributed fluorophores returning stochastically to their ground state. Use of conventional organic fluorophores provides a wide choice of probes that have a range of emission wavelengths, and such fluorophores are capable of emitting many photons before photobleaching, helping to improve the precision with which

Submitted December 9, 2010, and accepted for publication July 14, 2011.

*Correspondence: sam.hess@umit.maine.edu

Travis J. Gould's present address is Department of Cell Biology, Yale University School of Medicine, 333 Cedar Street, New Haven, CT 06510.

Editor: Anne Kenworthy.

© 2011 by the Biophysical Society

0006-3495/11/09/1522/7 $2.00

doi: 10.1016/j.bpj.2011.07.049

single molecules can be localized. Nevertheless, these methods sometimes rely upon some form of a reducing agent to maintain the desired residence time in bright and dark states (22), which may pose a major concern when applied to living cell imaging. Such limitations can be directly overcome by using genetically encodable fluorescent proteins that do not require any reducing agents during imaging and provide minimally invasive labeling (24).

Based upon the intensities of fluorescence detected in two spectral channels, Bossi et al. (17) demonstrated the first imaging examples of spectrally overlapping organic dyes in nonbiological samples. The method has been recently extended to four species in biological specimens (18). Nevertheless, thus far, it has been possible to image only up to two species using spectrally distinct PAFPs in fixed/living specimens (19–21). Some of these approaches may also require multiple excitation wavelengths for readout and may require sequential imaging (a limitation in the case of live-cell imaging). To facilitate simultaneous three-color FPALM imaging of biological samples such as fixed and live cells expressing three spectrally overlapping PAFPs within a narrow detection window (568–672 nm), we introduce PAmKate, a novel (to our knowledge) PAFP with far-red emission and other properties favorable for superresolution imaging, derived from mKate (25). We present the first, to our knowledge, simultaneous three-color images of live cells expressing three PAFP labeled proteins: 1), hemagglutinin (HA) (26), which has been associated with lipid rafts (27) and was tagged with Dendra2 (28); 2), actin tagged with PAmCherry1 (20); and 3), non-raft-associated transferrin receptor (29) (TfR) tagged with PAmKate in mouse fibroblasts (NIH-3T3 or HAb2). Fixed-cell images are also presented. We further discuss the observed correlations between plasma membrane components and cytoskeletal proteins based on both fixed- and live-cell results.

METHODS

See the Supporting Material and Fig. S1.

RESULTS

To convert mKate into a PAFP, we mutated amino acid residues at positions 69, 84, 148, 165, 167, 181, and 203 (numbering follows the alignment with green fluorescent protein (GFP) (see Fig. S2 in the Supporting Material), which were crucial for photoactivation of the chromophore in PAmCherry1. A bacterial library of the mKate mutants was screened with a fluorescence-activated cell sorter after illumination with a 405-nm LED array, after which colonies were selected on petri dishes using a fluorescence stereomicroscope. As a result, we found a PAmKate variant that contained substitutions F84W/S148N/S165G, as compared to mKate (see Fig. S2), and exhibited the most far-red-shifted emission among the mutants.

Before photoactivation, purified PAmKate had an absorbance maximum at 442 nm and did not fluoresce when excited at this wavelength. After photoactivation with 405 nm, the absorbance peak at 442 nm disappeared and an absorbance peak at 586 nm developed (see Fig. 1 *a*). These data suggest that PAmKate has a novel mechanism of photoactivation that differs from those described for PAmCherry1 (30) and PATagRFP (21). The photoactivation mechanism for PAmKate possibly consists of a light-driven transition of a neutral form of the DsRed-like chromophore (31) to its anionic fluorescent form. In the photoactivated state, the PAmKate exhibited far-red fluorescence with excitation/emission peaks at 586/628 nm, respectively. The measured molar extinction coefficient and quantum yield of the photoactivated PAmKate protein were 25,000 M^{-1} cm^{-1} and 0.18, respectively (see Table 1). The red state of PAmKate was stable with time, indicating that the photoconversion reaction

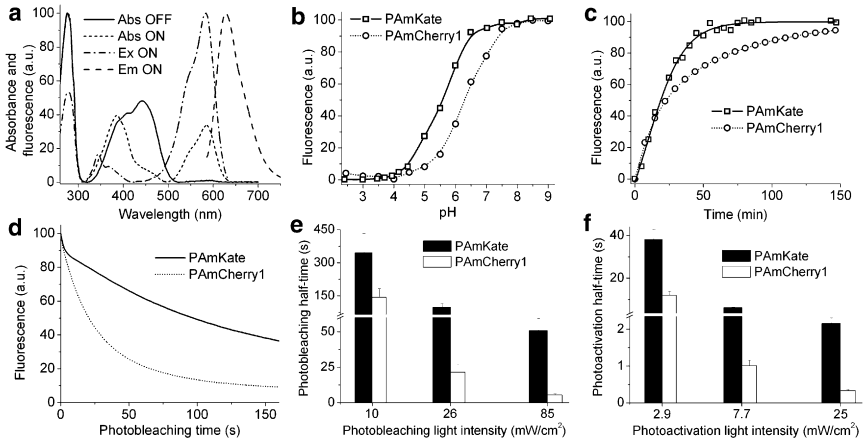

FIGURE 1 Spectral and biochemical properties of the purified PAmKate protein at room temperature. (*a*) Absorbance spectrum before photoactivation with 405-nm LED array (*solid line*), and absorbance (*short-dashed line*), excitation (*dash-dotted line*), and emission (*dashed line*) spectra after activation. (*b*) Equilibrium pH dependence for the fluorescence of PAmKate (*squares*) and PAmCherry1 (*circles*). (*c*) Maturation kinetics for the indicated proteins at 37°C. (*d*) Photobleaching kinetics for PAmKate (*solid line*) and PAmCherry1 (*dotted line*) at 26 mW/cm^2. (*e*) Photobleaching half-times for PAmKate (*solid columns*) and PAmCherry1 (*open columns*) at different power densities. (*f*) Photoactivation half-times for PAmKate (*solid columns*), and PAmCherry1 (*open columns*) at different power densities. In *d–f*, protein properties were measured in aqueous drops in oil using an Olympus IX-81 inverted microscope equipped with a 200-W metal-halide lamp, 100× 1.4 NA oil objective lens, and 570/30 nm (*d* and *e*) or 390/40 nm (*f*) excitation filters. The power densities were measured at the rear aperture of the objective. The photobleaching data (*d* and *e*) were normalized to the spectral output of the lamp, transmission profile of the filter and dichroic mirror, and absorbance spectra of the proteins.

TABLE 1 In vitro ensemble characteristics of PAmKate after photoactivation compared to other PAFPs and parent mKate

Protein	PAmKate	PAmCherry1	Dendra2	mKate
Type of photoconversion	Dark to red	Dark to red	Green to red	None
Absorbance peak (nm)	586	564	553	588
Extinction coefficient (M^{-1} cm^{-1})*	25,000	18,000	(35,000)	(31,500) 39,000
Emission peak (nm)	628	595	573	635
Quantum yield	0.18	0.46	(0.55)	(0.28)
Brightness relative to mKate (%)	41	76	(176)	100
p*K*a	5.6	6.3	(6.9)	(6.0) 6.9
Maturation half-time at 37°C (min)	19	23	(90)	22
Photobleaching half-time (s)†	100 ± 20	21 ± 6	ND	ND
Photoactivation half-time (s)‡	6.3 ± 0.2	1.0 ± 0.2	ND	ND
Photoactivation contrast (fold)	100	4000	300	ND

Dendra2 and mKate characteristics are taken from the articles in which they were introduced (shown in parentheses) or measured in our laboratory using the same conditions as for PAmKate.

*Characteristics were determined at the maximally achievable level of the photoactivated fluorescence signal using the conditions described in Fig. 1 *e*.

†Determined at 26 mW/cm^2 (570/30 nm filter) at the rear aperture of the 100× 1.4 NA oil objective lens.

‡Determined at 7.8 mW/cm^2 (390/40 nm filter) at the rear aperture of the 100× 1.4 NA oil objective lens. ND, not determined.

was irreversible. We then compared PAmKate to the well studied PAmCherry1. The fluorescence of PAmKate exhibited higher pH stability than that of PAmCherry1, with an apparent pK_a value of 5.6 (see Fig. 1 *b*). The maturation half-time for PAmKate was 19 min at 37°C (see Fig. 1 *c*), which is 1.2-fold faster than that of PAmCherry1. At 26 mW/cm^2 intensity of photobleaching light in a widefield microscope, the far-red fluorescence of PAmKate photobleached 4.6-fold slower than that of PAmCherry1 (see Fig. 1 *d*). The difference in photostability between PAmKate and PAmCherry1 reduced with decreasing power of the photobleaching light (see Fig. 1 *e*). At the highest tested intensity of photoactivation light (25 mW/cm^2), PAmKate had photoactivation kinetics 6.5-fold slower than that of PAmCherry1 (see Fig. 1 *f*). Decreasing the power of the photoactivation light reduced the difference in the photoactivation half-times for these proteins.

Addition of a dichroic mirror to the detection path of a standard FPALM geometry (see Fig. S1, Fig. S3) makes it possible to split the emission wavelengths contained within ~100 nm into two separate spectral windows and to record single-molecule intensities in two separate regions (channels) on a sensitive charge-coupled device. The relative intensity measured in a given channel depends on the probe emission spectrum. We introduce a relative intensity ratio (α) for a detected single molecule to capture such probe-dependent intensity variations on respective channels and define the ratio α as

$$\alpha = \frac{I_T}{I_T + I_R}, \tag{1}$$

where I_T and I_R denote the single-molecule intensities measured in channels T (transmitted) and R (reflected) (see Fig. S1), respectively. The ratio of the emitted fluorescence of a given species is dependent on the emission spectral overlap with each channel. Therefore, if the emission spectral distribution of a given species remains a constant, the relative fraction of emitted fluorescence on each channel would also remain a constant, and hence also the relative intensity ratio α. Since the emission peaks of photoactivated Dendra2, PAmCherry1, and PAmKate are at 573, 595, and 628 nm, respectively (see Table 1), the differences in emission spectra result in distinct values of α. However, due to photon counting and background noise, α for a given probe becomes a distribution of values (see Fig. 2 *f*). After uncertainty analysis on Eq. 1, the standard deviation of α in the presence of noise is given by

$$\left(\frac{\delta\alpha}{\alpha}\right)^2 = \left(\frac{\delta I_T}{I_T}\right)^2 + \frac{\delta I_T^2 + \delta I_R^2}{(I_T + I_R)^2}, \tag{2}$$

where δ signifies the standard deviation of a given variable. For 500 total photons detected from a Dendra2 molecule divided equally on channels T and R and a background noise of ~2.5 photons/pixel, the estimated standard deviation $\delta\alpha$ is 0.081, in close agreement with the value of 0.078 for the measured standard deviation of the Gaussian shaped α distribution for Dendra2-HA (see Fig. 2 *f*). The α distribution width of a species determines how different in α value a neighboring species should be for minimal interspecies α-distribution overlap. Therefore, the widths of α distributions will ultimately determine how many species are able to be imaged using the chosen detection channels. For background noise values of ~1.0 and ~4.0 photons/pixel, the estimated standard deviations, $\delta\alpha$, will be ~0.041 and ~0.086, respectively. Therefore, to minimize interspecies α distribution overlap and hence probe misidentification, considerable care needs to be taken to reduce background noise (using low background imaging buffer and objective immersion liquid) and to carefully choose probes and detection optics. The optical configuration presented has room in α space to fit at least two more species between 0.0 and 0.4 with more

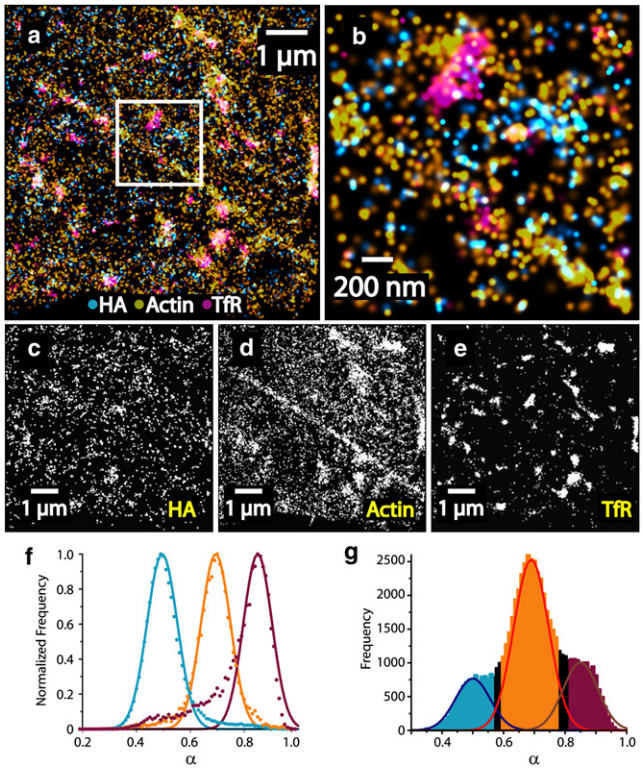

FIGURE 2 Three-color FPALM images of Dendra2-HA, PAmCherry1-β-actin, and PAmKate-Tfr expressed in fixed HAb2 mouse fibroblast cells. (*a*) Dense small clusters of transferrin receptor (*magenta*), more distributed clusters of HA (*cyan*), and the network of actin (*yellow*) throughout the cell and enriched at the cell edge. Scale bar, 1 μm. The image comprises localized identified molecules of Dendra2 (3,835), PAmCherry1 (11,044), and PAmKate (5,358). (*b*) Zoom-in of Dendra2 (322), PAmCherry1 (955), and PAmKate (266) localized molecules in boxed region in *a*. Scale bar, 200 nm. (*c–e*) HA molecules only (*c*), actin molecules only (*d*), and Tfr molecules only (*e*) in region depicted in *a*. (*f*) Measured distribution of relative intensity ratio α (*dots*) and Gaussian fits (*solid lines*) for individual fluorescent proteins Dendra2 (*cyan*), PAmCherry1 (*yellow*), and PAmKate (*magenta*). (*g*) Measured distribution of relative intensity ratio α (*shaded areas*) and the respective Gaussian fits (*solid lines*) for all three fluorescent proteins localized during acquisition of image *a*, identified as Dendra2 (*cyan*), PAmCherry1 (*yellow*), and PAmKate (*magenta*), as well as excluded molecules (*black*).

yellowish emission spectral peaks and possibly one more in the 0.9–1.0 range with a more red-shifted emission peak than PAmKate. However, to excite the more yellow probes may require a shorter readout wavelength. The prospect of engineering photoactivatable probes having more red-shifted emission spectra and larger Stokes shifts will help increase the number of detectable species using similar multicolor-fluorescence-detection approaches.

Frequently, a modest fraction of PAmKate molecules were observed to be already activated without any activation illumination. As a consequence, the initial single-species α distribution for PAmKate was skewed toward lower α values due to increase in the background noise. To minimize additional misidentifications caused by such effects, several methods were utilized. In fixed cell imaging, the molecules localized in the frames without activation illumination (the first thousand frames; see Table S1) were separated out, and only the molecules having an α ratio >0.8 were chosen for identification. In live cells, the visible preactivated PAmKate molecules were allowed to bleach at the start of acquisition.

Rendered fixed-cell images (see Fig. 2 *a*) show TfR forming dense clusters (also see Fig. 2 *e*), with a variety of compact shapes and sizes (100 nm to 1 μm) and each cluster covering ≤ 1 μm^2 in area, whereas in general, larger HA clusters were observed to be spatially well separated from clusters of TfR. The measured pair-correlation values, $g_{ab}(r)$, in fixed cells ($n = 11$) for $r = 0$–30 nm are 3 ± 2 for actin-TfR, 0.6 ± 0.8 for HA-TfR, and 1.8 ± 0.3 for actin-HA. These values suggest that both TfR and HA are correlated with actin, whereas TfR and HA are uncorrelated or anticorrelated.

The lack of colocalization between HA and TfR for the first time directly shows that a raft and nonraft protein do in fact have different nanoscale distributions. Pronounced actin distributions were visible along the cell edge and distributed around HA and TfR clusters. Actin is known to mediate membrane structure (33); regions of actin correlated with either HA or TfR were frequently evident (see also Fig. S4). It is intriguing that although HA and actin, and TfR and actin, are frequently colocalized, HA and TfR are generally not colocalized. It is also worth noting that the actin distributions sampled did not always produce linear structures. Such observations are consistent with the fact that genetically encoded protein tags labeled both globular (G) and filamentous (F) actin, as seen by the comparison of overlaid confocal images of both PAmCherry actin and Phalloidin labeling (Fig. S8), and are due to the fact that the part of the cell imaged was often the membrane proximal portion rather than the cell interior. In the live-cell experiments, TfR was often seen to arrange itself along linear tracks, mainly due to relatively rapid motion of TfR molecules, whereas in fixed cells, it was mostly arranged in dense circular clusters (Fig. S9, Fig. S10). Preactivation of PAmKate also reduced the sampling of PAmKate clusters visible initially. Therefore, the differences between the PAmKate-TfR distributions in live cells and those in fixed cells can be understood.

The dynamic renderings of the localization coordinates for live cells revealed TfR molecules moving much faster compared to HA and following linear tracks (see Fig. 3, Fig. S5, and Movie S1). The dense clusters of TfR observed frequently in fixed cells were less frequently observed in live cells due to the highly dynamic motions of TfR molecules. The HA clusters formed a variety of dynamically changing shapes. Some clusters were observed to diffuse, whereas others appeared to be constrained in motion (see Movie S1). Also, it was interesting to note that in some cases there existed dynamically varying nanoscale zones

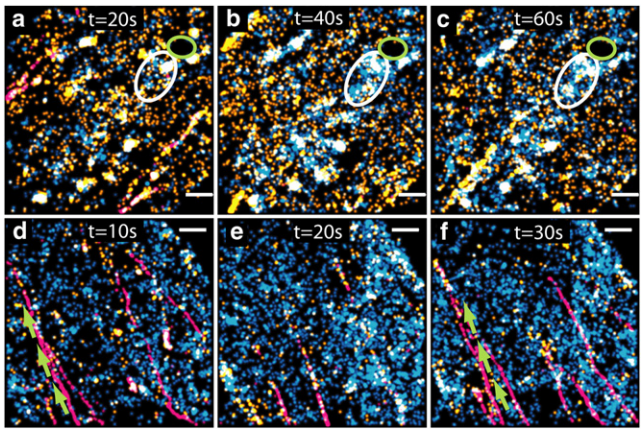

FIGURE 3 Three-color FPALM images of live fibroblast cells expressing Dendra2-HA (*cyan*), PAmCherry1-β-actin (*yellow*), and PAmKate-TfR (*magenta*). Renderings in *a–c* show molecules localized every 20 s. Circles in white show persistent high-density HA and actin regions, whereas circles in green highlight the existence of dynamic microdomains inaccessible to imaged molecules. Renderings in *d–f* (rendered molecules were localized every 10 s) show evidence of linear tracks (*green arrows*) on which Tfr (*magenta*) molecules travel. The dense small clusters of TfR often seen in fixed-cell images were less frequent. Scale bar, 1 μm. (For additional live-cell images, see the Supporting Material.)

that were inaccessible to all three species imaged (see Fig. 3).

DISCUSSION

We have described PAmKate, a novel photoactivatable protein and the farthest red-shifted PAFP reported to date, with an emission peak at 628 nm that facilitates simultaneous imaging of three spectrally overlapping PAFPs using the superresolution microscopic method FPALM in live and fixed cells with a single readout excitation wavelength. The method was successfully demonstrated on mouse fibroblasts expressing Dendra2-, PAmCherry1-, and PAmKate-tagged proteins labeling the plasma membrane and cytoskeleton.

Inspired by the work of Bossi et al. (17), the method presented here has been successful in simultaneously imaging three species in living cells. The recent GSDIM-based four-color superresolution method (18) is a major advance for fixed-cell imaging, yet has not been demonstrated for more than two species in a live specimen. Since the method demonstrated here uses photoactivatable proteins, no additional sample preparation methods such as SNAP tag technology or mounting media such as PVA (17,18) is required. Using a more red-shifted wavelength range (568–672 nm) for detection allowed us to limit autofluorescence (and hence the background noise) in the detected signal and to achieve the reported localization precisions (see also Fig. S6, Fig. S7). This is useful in the case of widefield illumination, since approaches such as TIRF, which limit the penetration depth of illumination light into the sample and therefore limit imaging more than a few hundred nanometers into the sample, may otherwise be required to keep the background noise levels low. The ability to image using widefield illumination with manageable background levels also allows straightforward extension of these methods to three dimensions. Also, it should be noted here that each species should be optimally transfected such that comparable amounts of each species are imaged. If not, the relative intensity ratio (α) distribution for the least numerous species may be overshadowed by a highly sampled neighboring species distribution.

The cell plasma membrane consists of a wide variety of lipids and proteins requiring specific organization to perform many important cellular functions, such as cholesterol transport, endo- and exo-cytosis, and signal transduction (34). Many models have been proposed to explain membrane organization, whereas the concept of rafts (fluctuating nanoscale assemblies of sphingolipids, cholesterol, and certain proteins) (35) has been instrumental in explaining many cellular functions. Defined by the detergent-resistant membrane (DRM) fraction, the liquid ordered and disordered phases of a plasma membrane constitute the raft and nonraft domains, respectively. However, concerns that DRMs do not represent intact biological membranes have incited controversy about the existence of rafts. The recent advent of superresolution microscopy has opened a way to directly test such concepts.

The considerable heterogeneity observed in the organization of the raft- and nonraft- associated proteins in both fixed and living specimens has also piqued interest in the role of the cytoskeleton played in membrane organization (33). Our choice of the raft and nonraft proteins HA and TfR along with actin was aimed at testing the role of the actin cytoskeleton in regulating membrane organization. The FPALM images of the fixed cells show colocalization of both HA and TfR with actin and cannot be explained by a simple raft-/nonraft model of membrane organization. Rather, this finding suggests that investigation of the specific interactions between membrane proteins and actin would be fruitful for understanding their membrane distributions. Efficient and selective removal of plasma membrane proteins from the cell surface can be done through endocytic uptake by clathrin-coated vesicles (36). The rapid movement of TfR observed in the live-cell experiments seems to suggest that the rapidly moving TfR molecules have already been associated with such clathrin-coated vesicles on early endosomal tubules, as opposed to being associated with plasma-membrane-derived clathrin-coated vesicles and in the process of being transported to the lysosome for degradation or for recycling back to the plasma membrane. The linear tracks observed seem to be consistent with studies confirming the actin-dependent propulsion of endosomes (37), as well as with the known role of actin cytoskeleton during clathrin-mediated endocytosis (38,39).

Our simultaneous visualization of two membrane proteins and actin has further demonstrated the importance

of actin in membrane organization. These results warrant further investigation of actin and other membrane-bound proteins for specific interaction and involvement of actin in fundamental cell functions. Having the choice of using more red-shifted fluorophores in particular is advantageous due to the fact that autofluorescence (prevalent mostly in the spectrally blue-green regions) can be mostly avoided by detecting fluorescence in the far-red spectral region. It is worth noting that the fast diffusion of TfR and lower photobleaching probability of PAmKate have enabled us to track TfR-containing structures over periods of tens of seconds and lengthscales of many micrometers. The observed preactivation of PAmKate molecules causes them to constitute the majority of localized molecules during the initial frames of an acquisition (i.e., those frames acquired without activation-laser illumination). The observed width of the PAmKate single species α distribution (Fig. 2 *f*) is largely due to background noise, partly because of the relatively low photoactivation contrast of PAmKate. To minimize PAmKate misidentifications as a result of background, molecules with $\alpha < 0.8$ localized during initial frames (where background tends to be higher) were discarded. The loss of these initially fluorescent molecules with $\alpha < 0.8$ does reduce the number of detected PAmKate molecules, especially in fixed cells, but presents a minimal disadvantage in live-cell imaging due to the eventual motion of unbleached molecules into the region of illumination.

Our new capability to simultaneously image three protein species at the nanoscale can address biological questions of importance where improved resolution is crucial. Quantification of interactions between three species (e.g., association of a plasma membrane protein and a cytoskeletal protein as a function of a viral protein) often requires three-species imaging (two will be insufficient) when the local concentrations of species are strongly spatially heterogeneous or temporally variable. Considering the very narrow portion of the visible spectrum being used here, this method can, in principle, be extended to more than three species using additional probes with distinct spectral or photophysical character. This method can also be directly extended to three dimensions coupled to Biplane FPALM (12) or 3D STORM (11).

SUPPORTING MATERIAL

Ten figures, two tables, one movie, and an additional Materials and Methods section are available at http://www.biophysj.org/biophysj/supplemental/S0006-3495(11)00941-6.

We thank K. Gabor, D. Kim, M. Mason, and E. Allgeyer for laboratory assistance and P. Byard, B. Hopler, and T. Tripp for professional services.

This work was supported by grants AI65459 from the National Institute of Allergy and Infectious Diseases, GM073913 and GM094713 from the National Institute of General Medical Sciences, CHE0722759 from the National Science Foundation, MTAF 1106 and MTAF 2061 from the Maine Technology Institute, and start-up funds from the Maine Economic Improvement Fund.

REFERENCES

1. Schermelleh, L., R. Heintzmann, and H. Leonhardt. 2010. A guide to super-resolution fluorescence microscopy. *J. Cell Biol.* 190:165–175.
2. Hell, S. W. 2007. Far-field optical nanoscopy. *Science.* 316:1153–1158.
3. Gould, T. J., V. V. Verkhusha, and S. T. Hess. 2009. Imaging biological structures with fluorescence photoactivation localization microscopy. *Nat. Protoc.* 4:291–308.
4. Yildiz, A., J. N. Forkey, …, P. R. Selvin. 2003. Myosin V walks hand-over-hand: single fluorophore imaging with 1.5-nm localization. *Science.* 300:2061–2065.
5. Hess, S. T., T. P. K. Girirajan, and M. D. Mason. 2006. Ultra-high resolution imaging by fluorescence photoactivation localization microscopy. *Biophys. J.* 91:4258–4272.
6. Betzig, E., G. H. Patterson, …, H. F. Hess. 2006. Imaging intracellular fluorescent proteins at nanometer resolution. *Science.* 313:1642–1645.
7. Rust, M. J., M. Bates, and X. Zhuang. 2006. Sub-diffraction-limit imaging by stochastic optical reconstruction microscopy (STORM). *Nat. Methods.* 3:793–795.
8. Hess, S. T., T. J. Gould, …, J. Zimmerberg. 2007. Dynamic clustered distribution of hemagglutinin resolved at 40 nm in living cell membranes discriminates between raft theories. *Proc. Natl. Acad. Sci. USA.* 104:17370–17375.
9. Manley, S., J. M. Gillette, …, J. Lippincott-Schwartz. 2008. High-density mapping of single-molecule trajectories with photoactivated localization microscopy. *Nat. Methods.* 5:155–157.
10. Shroff, H., C. G. Galbraith, …, E. Betzig. 2008. Live-cell photoactivated localization microscopy of nanoscale adhesion dynamics. *Nat. Methods.* 5:417–423.
11. Huang, B., W. Q. Wang, …, X. Zhuang. 2008. Three-dimensional super-resolution imaging by stochastic optical reconstruction microscopy. *Science.* 319:810–813.
12. Juette, M. F., T. J. Gould, …, J. Bewersdorf. 2008. Three-dimensional sub-100 nm resolution fluorescence microscopy of thick samples. *Nat. Methods.* 5:527–529.
13. Gould, T. J., M. S. Gunewardene, …, S. T. Hess. 2008. Nanoscale imaging of molecular positions and anisotropies. *Nat. Methods.* 5:1027–1030.
14. Bates, M., B. Huang, …, X. Zhuang. 2007. Multicolor super-resolution imaging with photo-switchable fluorescent probes. *Science.* 317:1749–1753.
15. van de Linde, S., U. Endesfelder, …, M. Sauer. 2009. Multicolor photoswitching microscopy for subdiffraction-resolution fluorescence imaging. *Photochem. Photobiol. Sci.* 8:465–469.
16. Bock, H., C. Geisler, …, C. Eggeling. 2007. Two-color far-field fluorescence nanoscopy based on photoswitchable emitters. *Appl. Phys. B.* 88:161–165.
17. Bossi, M., J. Fölling, …, S. W. Hell. 2008. Multicolor far-field fluorescence nanoscopy through isolated detection of distinct molecular species. *Nano Lett.* 8:2463–2468.
18. Testa, I., C. A. Wurm, …, C. Eggeling. 2010. Multicolor fluorescence nanoscopy in fixed and living cells by exciting conventional fluorophores with a single wavelength. *Biophys. J.* 99:2686–2694.
19. Shroff, H., C. G. Galbraith, …, E. Betzig. 2007. Dual-color superresolution imaging of genetically expressed probes within individual adhesion complexes. *Proc. Natl. Acad. Sci. USA.* 104:20308–20313.
20. Subach, F. V., G. H. Patterson, S. Manley, J. M. Gillette, J. Lippincott-Schwartz, and V. V. Verkhusha. 2009. Photoactivatable mCherry for high-resolution two-color fluorescence microscopy. *Nat. Methods.* 6:153–159.
21. Subach, F. V., G. H. Patterson, …, V. V. Verkhusha. 2010. Bright monomeric photoactivatable red fluorescent protein for two-color super-resolution sptPALM of live cells. *J. Am. Chem. Soc.* 132:6481–6491.

22. Fölling, J., M. Bossi, …, S. W. Hell. 2008. Fluorescence nanoscopy by ground-state depletion and single-molecule return. *Nat. Methods.* 5:943–945.

23. Heilemann, M., S. van de Linde, …, M. Sauer. 2008. Subdiffraction-resolution fluorescence imaging with conventional fluorescent probes. *Angew. Chem. Int. Ed. Engl.* 47:6172–6176.

24. Fernández-Suárez, M., and A. Y. Ting. 2008. Fluorescent probes for super-resolution imaging in living cells. *Nat. Rev. Mol. Cell Biol.* 9:929–943.

25. Shcherbo, D., E. M. Merzlyak, …, D. M. Chudakov. 2007. Bright far-red fluorescent protein for whole-body imaging. *Nat. Methods.* 4:741–746.

26. Ellens, H., J. Bentz, …, J. M. White. 1990. Fusion of influenza hemagglutinin-expressing fibroblasts with glycophorin-bearing liposomes: role of hemagglutinin surface density. *Biochemistry.* 29:9697–9707.

27. Scheiffele, P., A. Rietveld, …, K. Simons. 1999. Influenza viruses select ordered lipid domains during budding from the plasma membrane. *J. Biol. Chem.* 274:2038–2044.

28. Gurskaya, N. G., V. V. Verkhusha, …, K. A. Lukyanov. 2006. Engineering of a monomeric green-to-red photoactivatable fluorescent protein induced by blue light. *Nat. Biotechnol.* 24:461–465.

29. Harder, T., P. Scheiffele, …, K. Simons. 1998. Lipid domain structure of the plasma membrane revealed by patching of membrane components. *J. Cell Biol.* 141:929–942.

30. Subach, F. V., V. N. Malashkevich, …, V. V. Verkhusha. 2009. Photoactivation mechanism of PAmCherry based on crystal structures of the protein in the dark and fluorescent states. *Proc. Natl. Acad. Sci. USA.* 106:21097–21102.

31. Lukyanov, K. A., D. M. Chudakov, …, V. V. Verkhusha. 2005. Innovation: photoactivatable fluorescent proteins. *Nat. Rev. Mol. Cell Biol.* 6:885–891.

32. Reference deleted in proof.

33. Fujiwara, T., K. Ritchie, …, A. Kusumi. 2002. Phospholipids undergo hop diffusion in compartmentalized cell membrane. *J. Cell Biol.* 157:1071–1081.

34. Lingwood, D., and K. Simons. 2010. Lipid rafts as a membrane-organizing principle. *Science.* 327:46–50.

35. Simons, K., and E. Ikonen. 1997. Functional rafts in cell membranes. *Nature.* 387:569–572.

36. van Dam, E. M., and W. Stoorvogel. 2002. Dynamin-dependent transferrin receptor recycling by endosome-derived clathrin-coated vesicles. *Mol. Biol. Cell.* 13:169–182.

37. Taunton, J., B. A. Rowning, …, C. A. Larabell. 2000. Actin-dependent propulsion of endosomes and lysosomes by recruitment of N-WASP. *J. Cell Biol.* 148:519–530.

38. Qualmann, B., M. M. Kessels, and R. B. Kelly. 2000. Molecular links between endocytosis and the actin cytoskeleton. *J. Cell Biol.* 150:F111–F116.

39. Yarar, D., C. M. Waterman-Storer, and S. L. Schmid. 2005. A dynamic actin cytoskeleton functions at multiple stages of clathrin-mediated endocytosis. *Mol. Biol. Cell.* 16:964–975.